Journal of Statistical Physics, Vol. 54, Nos. 5/6, 1989

Noise-Induced Intermittency in the Quasiperiodic Regime of Rayleigh–Bénard Convection

Robert Ecke[1] **and Hans Haucke**[1,2]

Received September 30, 1988

Thermal measurements on a convecting dilute ^{3}He–superfluid ^{4}He solution in the quasiperiodic regime show a transition from a mode-locked periodic state to chaotic time dependence via intermittency. The type of intermittency is discussed in the context of standard models of the phenomenon. In a region just below the onset of intermittency, injection of external multiplicative noise with noise amplitude above a certain threshold level induces the chaotic state. This noise-induced transition can be understood to be due to perturbations of a system with a barely stable attractor; the noise causes the system to escape the weakly attracting periodic points. We present a numerical simulation of a 1D map with external noise which explains some aspects of the noise-induced behavior, and a 2D map which has certain features of the intermittency.

KEY WORDS: Intermittency; noise-induced transition; thermal convection; quasiperiodicity.

1. INTRODUCTION

The application of external noise to a system which is close to a bifurcation from a stable state to a chaotic attractor can have dramatic effects. We experimentally study the transition, in a thermally convecting fluid, from a mode-locked periodic state to an intermittently chaotic state and the effects of multiplicative (parametric) noise on this transition. Intermittency, defined as the presence of regular or "laminar" intervals interrupted by chaotic bursts, is a common route to chaos in low-dimensional systems. It can occur in both the period-doubling and circle maps after the initial chaotic transition.[1,2] Intermittency has been found experimentally in elec-

[1] Physics Division and Center for Nonlinear Studies, Los Alamos National Laboratory, Los Alamos, New Mexico 87544.

[2] Present address: IBM T.J. Watson Research Center, Yorktown Heights, New York.

0022-4715/89/0300-1153$06.00/0 © 1989 Plenum Publishing Corporation

tronic circuits[3] and in other convection work, including that of Bergé, Dubois, and co-workers[4] using silicone oil. Theoretical work by Eckmann *et al.*[5] on one type of intermittency indicates that noise can induce such a transition prematurely. Previously, we briefly reported results for a noise-induced transition to intermittency in convecting ^{3}He–superfluid ^{4}He mixtures.[6] In this paper we expand that description in the light of additional data and present further analysis of the transition from a mode-locked periodic state to one of intermittent chaos, presumably involving global bifurcations resulting from the overlap of resonance horns.

We have found that the application of noise to our convection cell leads to simple but surprising results. Our convective system can be driven into a chaotic regime by the application of external Gaussian broadband noise, the transition occurring at a well-defined nonzero noise level. According to theoretical models, the noise induces random-walk fluctuations which, after some period of time, may be sufficiently large to drive the system into an unstable regime. This effect is balanced by dissipation of the noise-induced fluctuations owing to the attractive (albeit weakly) nature of the stable state. The slow response of the system near the intermittent onset provides for long averaging times and the experimentally observed sharp noise threshold. Before presenting details of the experiment and results with applied external noise we will give a general description of the quasiperiodic regime in which this transition takes place. This region has been explored extensively by us in a number of experiments[7,8] and a description of features of this region is helpful in understanding the noise-induced phenomena.

Thermal convection in dilute solutions of ^{3}He in superfluid ^{4}He very closely approximates classical Rayleigh–Bénard convection in a classical single-component fluid.[9,10] For the purposes of convection the dilute solutions have an effectively negative thermal expansion coefficient and a low and variable Prandtl number (defined as the ratio of kinematic viscosity to thermal diffusivity, ν/κ) in the range 0.04–0.2. The negative expansion coefficient implies that one must heat the fluid from the top to induce convection. This behavior is a result of superfluid counterflow which pushes ^{3}He atoms away from the hotter boundary. The ^{3}He is lighter than the surrounding ^{4}He and when pushed down by counterflow produces a gravitationally unstable density gradient. At some critical temperature difference the fluid begins to convect. This transition is best described in terms of a dimensionless parameter, the Rayleigh number, defined as $R = g\alpha d^3 \Delta T/\nu\kappa$, where g is the acceleration due to gravity, α is the effective themal expansion coefficient, d is the depth of the fluid layer, ΔT is the temperature difference across the layer, ν is the kinematic viscosity, and κ is the thermal diffusivity. For a laterally infinite fluid layer, convection begins at

$R_c = 1708$, whereas for finite geometries, particularly those with small aspect ratio, convection typically begins at a somewhat higher value.

The parameter space of single-component convection is defined, within the Boussinesq approximation, in terms of the Rayleigh number R, the Prantdl number Pr, and the cell geometry, which is fixed and rectangular in this experiment with height $d = 0.8$ cm, length $2.0d$, and width $1.4d$. The Rayleigh number is controlled by varying the temperature difference across the layer and the Prandtl number is roughly proportional to the mean cell temperature, which can vary between 0.6 and 1.5 K.

The bifurcations which occur in the parameter space formed by Pr and R are shown in Fig. 1. For $R < R_c$ the fluid conducts heat diffusively, while above R_c there is a stationary velocity field which convects heat across the layer, thereby enhancing heat transport.[10] The next instability is a forward Hopf bifurcation to oscillatory convection.[11] The value of R at which this transition occurs is highly Prandtl number dependent, as opposed to R_c, which is independent of Pr to within experimental uncertainty.[10] Another Hopf bifurcation occurs at higher Rayleigh number, leading to a regime characterized by two incommensurate frequencies; the spectral content of a time series from the system in this region can typically only be described by two frequencies not related by the ratio of integers. Within the two-frequency region there is significant interaction between the hydrodynamic modes responsible for the two frequencies. This interaction results in mode locking and an ordering of mode-locked intervals in a devil's staircase; see Fig. 2. A parameter that characterizes this mode locking is the winding number W, which is defined here as the ratio of the fundamental frequen-

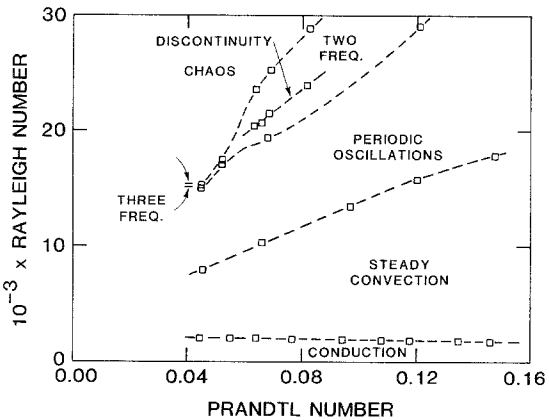

Fig. 1. Phase diagram of the convection system in Rayleigh number—Prandtl number space. Different states include thermally diffusive conduction, time-independent convection, periodic oscillations, two-frequency quasiperiodicity, three-frequency quasiperiodicity, and chaos.

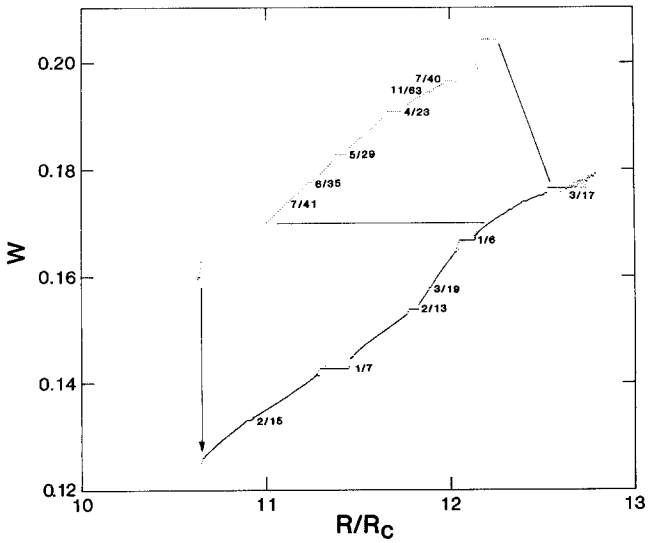

Fig. 2. Winding number W versus normalized Rayleigh number with a bottom-plate temperature of 0.8500 K. The "steps" indicate mode locking. The upper central portion of the figure is a blowup of the main curve to illustrate finer detail. All lockings are labeled with thier winding number values.

cies of the two modes; when the modes are locked this number takes on a rational value, i.e., the ratio of two integers.

In the parameter space of Rayleigh and Prandtl number the locked regions form resonance horns which become wider as the Prandtl number is reduced. Figure 3 shows the major horn with winding number 2/13 and also shows the structure within the horn arising from the breakdown of the torus. One of the main features which is observed in the middle of the resonance horn is a transition from period-2 points to small secondary tori, indicating a Hopf bifurcation of the period-2 attractor. As Pr is reduced, these secondary tori become unstable and undergo lockings, period doublings, and chaotic intermittent cycling between the small tori. Details of this structure have been reported elsewhere.[8,12] As Rayleigh number is increased (or Pr reduced), resonance horns persist but become increasingly surrounded by chaotic intervals. Eventually there are no longer any locked regions and the system is chaotic everywhere. For the data we report here there is a locked interval with winding number 2/11 surrounded by chaotic intervals above and below in Rayleigh number. As in ref. 8 and 12, we observe internal structure within the horn, namely that as Rayleigh number is increased across the horn the stable period-2 cycle of the 2/11 locking goes to a period-6 secondary Hopf structure (in other words, each point of

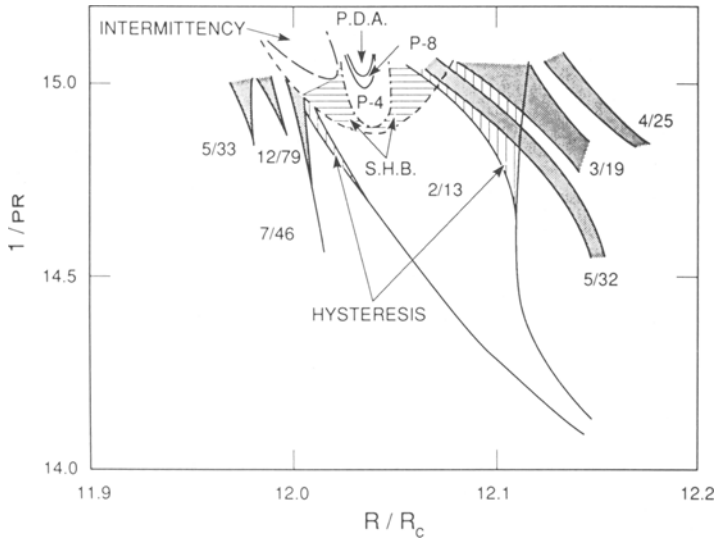

Fig. 3. Inverse Prandtl number $1/Pr$ versus normalized Rayleigh number R/R_c showing a large resonance horn with $W = 2/13$. Regions of hysteresis, secondary Hopf bifurcation (SHB), period doublings (P-4 and P-8) and accumulation (PDA), and intermittency are indicated. Other resonance horns, some of which overlap the 2/13 horn, are also labeled.

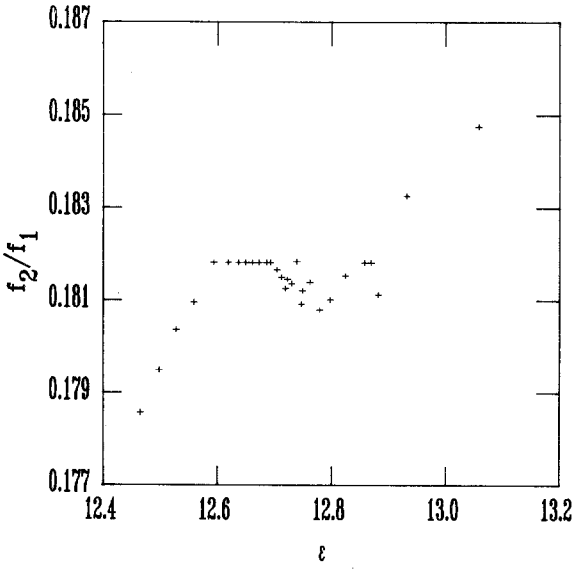

Fig. 4. Winding number f_2/f_1 versus stress parameter $\varepsilon \equiv R/R_c - 1$ showing one cut ($1/Pr \simeq 14.7$) through the 2/11 ($W = 0.181818...$) resonance horn. The scatter of W in the interior of the horn indicates chaotic behavior.

the stable 2-cycle gives rise to three small circles in the Poincaré sections). There is then a region of intermittent chaos in the middle of the locking and finally the period-2 cycle reappears at the upper edge of the horn. Figure 4 shows the winding number for this region and illustrates the chaos in the middle of the horn in the scatter of the winding number over that interval. (Although the winding number is in some sense not well defined in the chaotic interval, as evidenced by the scatter in Fig. 4, operationally one defines W as the ratio of the peak frequencies of the fundamentals, which are only distorted, not completely destroyed, by deterministic broadband noise arising from a chaotic state.) Before discussing the dynamics of this region in detail we will present the experimental procedure, the results of applying external noise, and a numerical simulation which helps explain some of the behavior we observe in the experiment.

2. EXPERIMENTAL RESULTS AND ANALYSIS

In operation, a constant heat flow $\dot{Q}$ is introduced to the top plate of the cell and the bottom plate is controlled at a fixed temperature of 0.850 K corresponding to a Prandtl number of 0.068. The temperature difference across the cell is ΔT, and the convective onset is at $\Delta T_c = 4.28$ mK. We define the stress parameter as $\varepsilon = \langle \Delta T \rangle / \Delta T_c - 1 = \langle R \rangle / R_c - 1$, with the angle brackets denoting a time average. In addition to measurements of the top–bottom temperature difference, we also had a probe which measured local temperature differences near the center of the top plate. This probe consisted of a small, thermally-insulated plug inserted in the top plate. The temperature difference between this plug and the rest of the top plate was measured with a gold–iron thermocouple whose current was sensed by a SQUID ammeter.[10] All time-dependent data reported in this paper were obtained from this local probe.

For part of this work we coupled an external noise source to the experiment. The primary sources of noise intrinsic to the apparatus were Johnson noise in the thermocouple and fluctuations in the bottom-plate temperature produced by variations in the cooling power of our ^{3}He evaporation refrigerator. Only the latter can affect the dynamics of the system. We chose to add broadband noise to the voltage applied to the bottom-plate heater, giving us a noise source with a character similar to the intrinsic experimental noise. The instantaneous output of our noise generator had a Gaussian distribution about zero voltage and a high-frequency cutoff of 50 Hz. The actual spectrum of the thermal fluctations of the bottom plate depended on the settings used for the bottom-plate temperature controller and on thermal time constants in the experiment. Measurements made on a simply periodic convective state showed that the

application of external noise in the manner described above simply increased the broadband noise floor and did not otherwise modify characteristics of the power spectrum; quantities such as the peak amplitude and frequency of the fundamental were unchanged, indicating that the application of external noise did not cause an effective shift in the Rayleigh number of the system. While in this state, we determined the relation between noise in the heater voltage and fluctuations in ΔT. Owing to feedback control of the bottom-plate temperature, the average value of ΔT was unaffected by the heater-voltage noise.

We define the noise amplitude σ as the normalized rms fluctuations in ΔT:

$$\sigma = \frac{\langle (\Delta T - \langle \Delta T \rangle)^2 \rangle^{1/2}}{\langle \Delta T \rangle} \tag{1}$$

This quantity includes both intrinsic and externally applied noise. The relation of σ to rms-applied-noise voltage determined in this state was assumed to apply during measurements of the chaotic state.

In detecting the transition from a stable periodic state to a chaotic state it is useful to have a simple method of quantifying the degree of "chaos" in a time series. Although methods such as fractal dimension, metric entropy, or Lyapunov exponent algorithms give a direct and theoretically useful measure of the degree of chaos,[13] they are somewhat cumbersome to implement. We have found a simple measure of the normalized broadband spectral power to be useful. This "noise-to-signal ratio" N/S is defined as

$$\frac{N}{S} = \frac{1}{f_2 - f_1} \int_{f_1}^{f_2} \log_{10} \frac{P(f)}{\bar{P}} \, \mathrm{df}, \qquad \bar{P} = \frac{1}{f_2 - f_1} \int_{f_1}^{f_2} P(f) \, df \tag{2}$$

where $P(f)$ is the power-spectral density of the probe temperature fluctuations and f is frequency. This quantity thus varies depending on the part of the spectrum averaged. Besides its extreme simplicitly, it is highly sensitive to changes in the spectrum even near the noise floor and is relatively insensitive to spectral resolution since sharp peaks contribute nothing in the limit of infinite resolution.

As discussed above, at the onset of convection ($\varepsilon = 0$) the fluid begins to move time independently. For $Pr = 0.068$, the first oscillatory instability occurs at $\varepsilon = 4.14$, with an amplitude that grows from zero as ε is further increased.[10,11] The second oscillation, also starting with zero amplitude, begins at $\varepsilon = 9.12$. Somewhat above $\varepsilon = 9.12$, nonlinear interactions between the two oscillations produce a number of regions of frequency locking and of chaos. In this region we focus on a resonance horn with winding

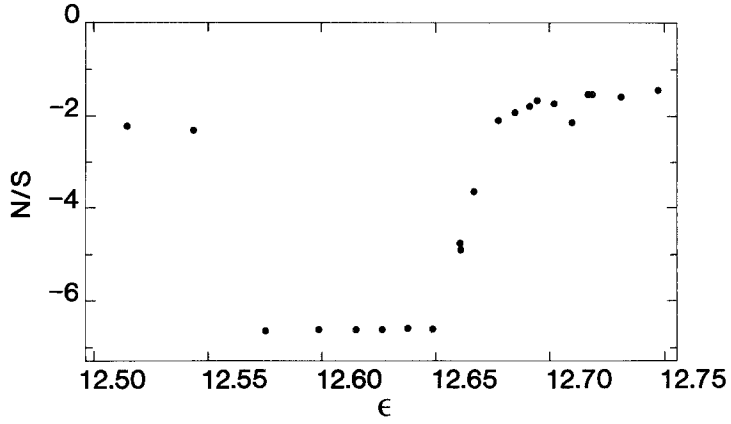

Fig. 5. The observed noise level, as characterized by N/S, plotted as a function of the stress parameter ε. The interval with small N/S values corresponds to the period-2 locked state.

number 2/11. This resonance horn is defined in Fig. 4 as the region $12.58 < \varepsilon < 12.86$, although the frequencies are not locked in the middle of the horn where chaotic states exist. In the interval $12.575 < \varepsilon < 12.648$ the two frequencies are locked in a 2/11 ratio; the lower frequency f_2 is about 0.13 Hz. Figure 5 shows the behavior of N/S over a somewhat larger range of stress parameter. Intermittent bursts, as illustrated in Fig. 6, are seen at

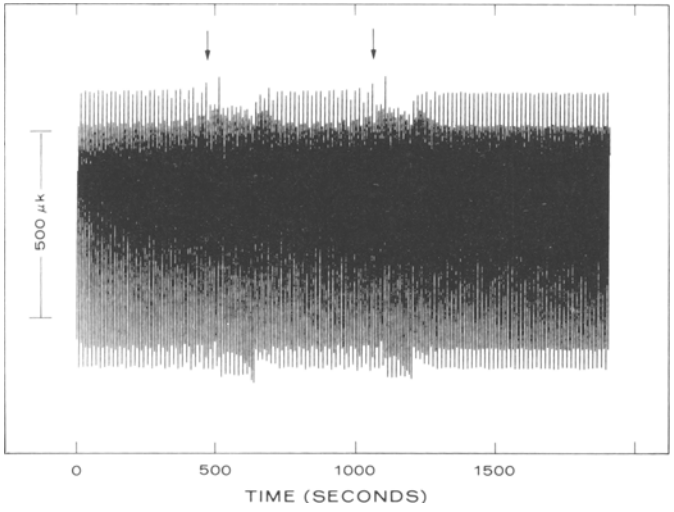

Fig. 6. A time series of temperature oscillations of the probe thermocouple just above the intermittent onset, with no external noise applied. The arrows indicate the region of slow buildup of the $f_2/6$ amplitude.

the upper end of the locked region, giving broadband noise increases of ~ 40 dB in power spectra. We will focus on this upper region in Fig. 5, which is in the middle of the 2/11 resonance horn. The burst rate increases as one moves away from the locked state until it is no longer possible to indentify any portion of the time series as displaying the simple behavior characteristic of the locked state. Both bursts and quiescent intervals are visible in Fig. 6.

One method of characterizing intermittent behavior is by the probability distribution of the lengths of quiet intervals, as in Fig. 7. This figure shows a histogram of the number of quiet intervals versus their length l. The length of a burst is defined in terms of a feature of the intermittent bursts which suggests something about the dynamics of the intermittency as discussed below. The bursts occur after a slow buildup of the $f_2/6$ amplitude, as may be discerned from Fig. 6. To see this, look at the maxima of the time series in Fig. 6. There are large-amplitude and somewhat smaller-amplitude excursions. Considering just the large-amplitude maxima, there is a period-3 growth of these peaks in a sequence small–large–large, the peak height difference increasing as the burst is approached. Taking into account both large and small maxima, the period is 6, corresponding to a frequency of $f_2/6$. Here f_2 is the lower of the two frequencies, and we define l to be the number of $f_2/6$ oscillations between bursts. These data were taken at $\delta = +0.005$, above the spontaneous onset and without external noise.

Near but below the upper end of the locked region we observed that intermittent behavior could be induced by applying noise to the system.

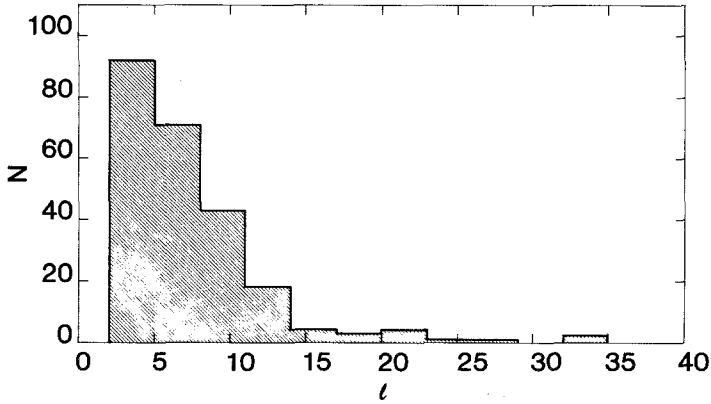

Fig. 7. A histogram of the number of burst-free intervals versus the length of those intervals; $\delta = +0.005$, above the spontaneous onset and with no external noise applied; l is the number of $f_2/6$ oscillations seen between bursts.

Figure 8 shows N/S versus σ for various values of δ, where $\delta \equiv \dot{Q}/\dot{Q}_0 - 1 \approx \varepsilon/\varepsilon_0 - 1$; the subscript indicates the value at onset, defined as that point where bursts occur with zero applied noise. The rise in N/S is caused by the presence of one or more bursts in a run (lasting about 1 hr). We see that a rather sharp threshold σ_c exists, above which bursts are induced and below which external noise simply adds to the intrinsic noise. At the highest noise levels, N/S appears to saturate at a smaller value. The dependence of σ_c on δ is shown in Fig. 9 and appears linear over the plotted range of δ.

The intermittent bursts seen in the time series and the accompanying rise in broadband noise are in qualitative agreement with Pomeau and Manneville's intermittency scenario.[1] Figure 7 shows a monotonic decrease of the probability of a quiet interval as its length increases, consistent with their type II or III intermittency; the exact form of the probability distribution may depend on the reinjection mechanism.[14] In contrast, type I intermittency produces bimodal histograms.[2] The effects of noise on type I intermittency have been studied numerically.[5] In particular, the rapid increases in N/S we observe in Fig. 8 are consistent with the calculations of Eckmann *et al.* (Fig. 7a of ref. 5), which indicate a very rapid variation in burst rate with small changes in applied noise. In the next section we discuss how this "noise threshold" effect carries over to maps characteristic of the other types of intermittency and how one can use

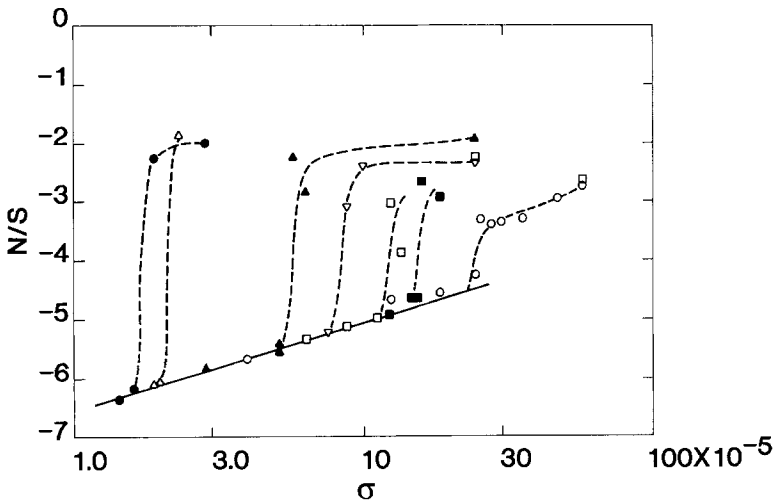

Fig. 8. Noise-to-signal ratio N/S versus external noise amplitude σ for various values of δ: open circles ($\delta = 8.4 \times 10^{-4}$), filled squares ($\delta = 6.7 \times 10^{-4}$), open squares ($\delta = 5.4 \times 10^{-4}$), inverted open triangles ($\delta = 3.8 \times 10^{-4}$), filled triangles ($\delta = 2.2 \times 10^{-4}$), open triangles ($\delta = 1.0 \times 10^{-4}$), and filled circles ($\delta = 0.4 \times 10^{-4}$). The solid line indicates the condition that input noise simply adds to the intrinsic noise. Dashed lines are guides to the eye.

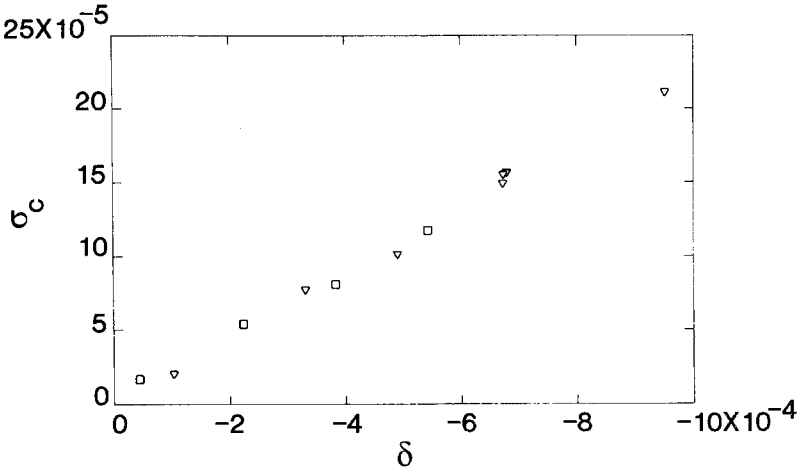

Fig. 9. The critical noise value for the onset of bursts σ_c plotted versus δ. Two different runs (squares and triangles) are shown, having onset values ε_0 different by 0.03%.

this effect to predict power-law relations between σ_c and δ. We then compare the predicted power-law behavior with the experimental results shown in Fig. 9.

3. NUMERICAL MODELS OF INTERMITTENCY

In this section we show numerical results illustrating the effects of noise on the mean laminar interval or time between bursts, l. We also present a heuristic argument for the scaling of l with the noise level and with the distance from the unperturbed bifurcation point. These results are partially contained in more rigorous and thorough treatments,[2,5] although the scaling and numerics for a cubic tangency are presented here explicitly for the first time. We follow ref. 2 and consider a map,

$$x_{n+1} = x_n + ax_n^2 + \delta + \sigma\xi_n \tag{3}$$

which is an expansion of the logistic map around a tangency point. This quadratic map applies for type I intermittency and has a stable and an unstable fixed point for $\delta < 0$, a tangent point when $\delta = 0$, and a fixed point at $x = \infty$ for $\delta > 0$. The map is assumed to have a reinjection mechanism away from the tangency modeled in Eq. (3) such as occurs in the logistic map but that is not important for determining the scaling of l. We use an additive noise term $\sigma\xi_n$ which is a random variable having a Gaussian distribution and a variance $\langle \xi^2 \rangle = 1$. (In the experiment the noise is mul-

tiplicative or parametric, but in 1D logistic map models this difference only comes in as higher-order correlations of the noise statistics and does not affect small-noise results.[15]) The variable δ measures the width of the near tangency and is a measure of how close the map is to the tangent bifurcation. To find $\bar{l}$ numerically, we iterate the map model of Eq. (3), and measure the length of time it takes the system to traverse a region near the tangency.

In order to see a clear relationship between the numerical results and the experimental data, it is useful to present the data in a scaled form so that all values of a, δ, and σ fall on the same curve. The proper scaling for a quadratic map was determined in ref. 5 and is reproduced here in a heuristic fashion; extension of our analysis follows easily for the cubic map case. If we make the assignments $c = (|\delta|/a)^{1/2}$ $\lambda = 2ac$, and $z = (x + c)/2c$ and substitute into Eq. (3), we find

$$\begin{aligned} z_{n+1} &= (1-\lambda)\, z_n + \lambda z_n^2 + a\sigma\xi_n/\lambda, & \delta < 0 \\ z_{n+1} &= (1-\lambda)\, z_n + \lambda z_n^2 + a\sigma\xi_n/\lambda + 2a\delta/\lambda, & \delta > 0 \end{aligned} \tag{4}$$

We then follow ref. 2 and use the approximation $z_{n+1} - z_n \sim dz/dt$. Next we rescale the time $t \to t' \equiv \lambda t$. The noise amplitude is simultaneously scaled as $\sigma \to \sigma\sqrt{\lambda}$ to account for the increased variance of the noise. This gives the equations

$$\begin{aligned} dz/dt' &= -(z - z^2) + a\sigma\xi/\lambda^{3/2}, & \delta < 0 \\ dz/dt' &= -(z - z^2) + a\sigma\xi/\lambda^{3/2} + 1/2, & \delta > 0 \end{aligned} \tag{5}$$

These Langevin equations can be solved by writing the corresponding Fokker–Planck equations for the time evolution of the probability distribution.[5] From a simpler perspective, however, one can see in Eqs. (5) that the result must be some function of $a\sigma/\lambda^{3/2}$, assuming that the endpoint conditions are sufficiently large that the scaling of x to z does not enter. Taking into account the time rescaling, the average bust time $\bar{l}$ follows as

$$\bar{l} = (1/\lambda)\, h(a\sigma/\lambda^{3/2}) \tag{6}$$

where h is some unknown function. This analysis should apply in the case $\lambda \ll 1$, $a\sigma/\lambda \ll 1$, and $\bar{l} \gg 1$. The first two conditions make the transition from iteration to differential equation plausible, and the last condition is required to ensure that the endpoints are far apart.

Although the derivation above is not rigorous, one test of its usefulness is in its success in scaling numerical data. In Fig. 10a we plot $\lambda\bar{l}$

versus $a\sigma/\lambda^{3/2}$ for various values of a, δ, and σ [recall $\lambda = 2(a\delta)^{1/2}$]. The value of $\bar{l}$ was determined by calculating the mean number of iterations needed to go from the initial point $x = -1/2$ to a value $x > 1/2$. The results of Fig. 10a show that the scaling behavior is as expected. In the absence of noise for $\delta > 0$ the length of a laminar period goes as $\delta^{-1/2}$ (i.e., $\bar{l}\lambda = \text{const.}$ in Fig. 10a). At small δ and large noise σ, the values for above and below the onset coincide, as they should. The slope for that region, in the lower right corner of the plot, is $-2/3$, as it must be to avoid singular behavior at $\delta = 0$. The portion of the plot extending vertically is the most relevant to our experimental results. This shows that the mean length of a laminar

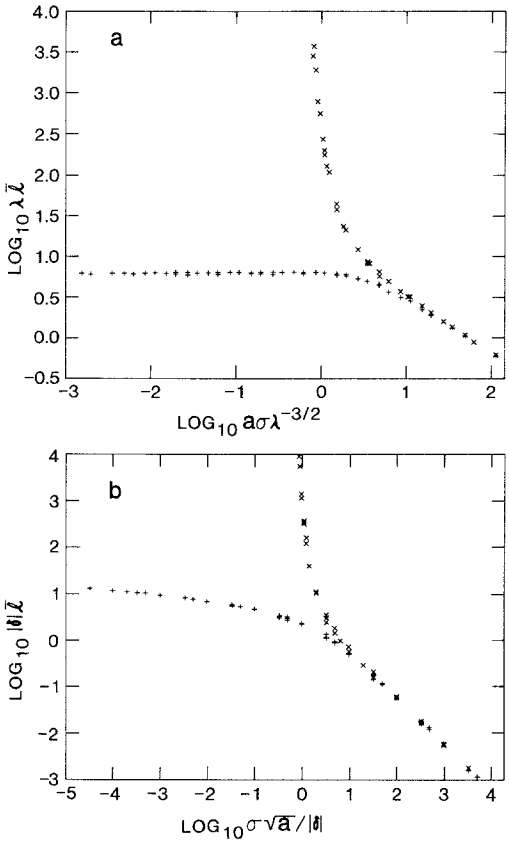

Fig. 10. (a) A log–log plot of $\bar{l}$, the time between intermittent bursts from the quadratic map of Eq. (3), versus noise amplitude σ, using the rescaled parameters $a\sigma\lambda^{-3/2}$ for noise and $\lambda\bar{l}$ for the mean time between bursts. (+) $\delta > 0$, (×) $\delta < 0$. (b) A log-log plot of the time between bursts for the cubic map, Eq. (7), versus noise amplitude δ, using rescaled variables $\sigma a^{1/2}/|\delta|$ for the noise and $|\delta|\,\bar{l}$ for the burst rate. (+) $\delta > 0$, (×) $\delta < 0$.

interval changes very rapidly as a function of $a\sigma/\lambda^{3/2}$. Therefore the critical noise threshold is approximately given by the condition $a\sigma/\lambda^{3/2} = \text{const.}$ which implies $\sigma \sim \lambda^{3/2} \sim \delta^{3/4}$. Qualitatively, this would explain the apparent sharp turn-on in observed noise as the applied noise is increased, as seen in Fig. 8.

Very similar behavior is found when the case of a cubic rather than a quadratic tangency is considered:

$$x_{n+1} = (1+\delta)\, x_n + a x_n^3 + \sigma \xi_n \tag{7}$$

This map is the type suggested for the case of intermittency of type II or III. Rescaling Eq. (7) as described above gives the relation $\bar{l} = (1/\delta) h(\sigma(a/\delta)^{1/2})$, where, as above, h is some unknown function. The

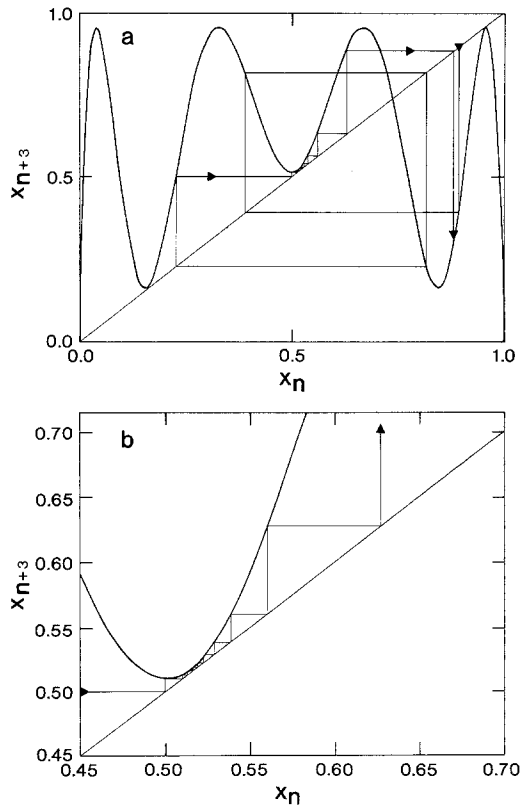

Fig. 11. (a) The third iterate of the map $x_{n+1} = r x_n (1 - x_n)$ for r just below the critical value $r_c = 1 + \sqrt{8}$ (this figure follows Fig. 4 of ref. 2). (b) An expanded view of the central tangency of Fig. 11a, with several iterations plotted (this figure follows Fig. 5 of ref. 2).

numerical results for the cubic case are shown in Fig. 10b. The vertical portion of the data in Fig. 10b suggests the approximate relation $\sigma_c \propto \delta$ for the cubic map, as opposed to the $\sigma_c \propto \delta^{3/4}$ for the quadratic map. Our data, shown in Fig. 9, seem to be in better agreement with the scaling for a cubic map.

To understand these models for intermittent behavior, one has to consider the "reinjection" process. The iterative maps of Eqs. (3) and (7) are no necessarily chaotic. For example, one can have a tangent bifurcation in a circle map. The time to traverse the region of tangency should be similar to that found for Eq. (3), but there is no chaotic behavior. The chaos in intermittency models is produced by chaotic behavior occurring not near the tangency, but in other portions of the map. A chaotic one-dimensional map must be noninvertible and thus have multiple values of x_n producing the same value of x_{n+1}. This allows points in distant portions of the map to be "injected" near the tangency. An example is shown in Fig. 11, for the third iterate of the logistic map $x_{n+1} = rx_n(1 - x_n)$. Also illustrated here is the manner in which the iteration of the map causes slowing down close to a near-tangency. The injection into the region of tangency has been modeled[2] by assuming a flat distribution of starting points within some range of x values straddling the tangency. This gives rise to a bimodal probability distribution for the lengths of the laminar intervals; the traversal times are short or long for injection to the left or right of the tangency. This bimodality is not in agreement with the experimental histogram plotted in Fig. 7, whereas the unimodal distribution expected for a cubic map does agree qualitatively with our data.

4. DYNAMICS OF THE OBSERVED INTERMITTENCY

It is important to demonstrate not only that scenarios like intermittency, period doubling, and mode locking occur, but that the models used are appropriate to the data. We have attempted to produce a return map from our data. This is the best method of determining the applicability of various numerical models. We have been unable to construct directly such a one-dimensional map, but examination of the Poincaré sections suggests something about the origin of the intermittency.

One obtains Poincaré sections consisting of two dots for Rayleigh numbers inside the 2/11 mode-locked interval in Fig. 4 and a portion of which is shown in Fig. 5 as the large region of low N/S. As R is increased past the upper edge of this region, each dot becomes three small circles, indicating a secondary Hopf bifurcation of the locked state in addition to some mechanism which takes a single point into three points. (We refer to these three circles as a period-3 cycle with respect to a single point, but

another way to describe them is as a period-6 cycle arising from the period-2 locked state.) A similar transition in the interior of the 2/13 horn is illustrated in Fig. 3 and discussed in detail in refs. 8 and 12. A precursor to this threefold splitting is found in very low-level $f_2/6$ subharmonics that exist in power spectra just below this transition. We do not understand the details of this transition nor its importance in understanding the transition to intermittency. The next state which we observe as Rayleigh number is increased is an intermittent state which is related to the period-3 secondary tori; the nonlaminar excursions occur in the vicinity of the previous positions of the period-3 tori. This is presumably due to a collision of the stable manifold of the small tori with the unstable manifold of the saddles which form the virtual separatrices of the period-3 tori. To understand this intermittency, we display in Fig. 12 a Poincaré section made just above the onset of intermittency, slightly beyond where we found the three circles. Here, those points have started to mix together. The intermittent chaos we observe is due to the irregular, aperiodic movement between circles. The points in Fig. 12a are labelled 1, 2, 3, 1, 2, ..., in order of their occurrence. A similar plot for the three circles would show the iteration proceeding in a regular way so that each circle would be composed of only 1's, 2's, or 3's. The solid lines in the figure show how the points iterate, connecting successive third iterate points, and should not be confused with trajectory lines. Along each sequence of these third iterate points is a region of high point density. In the high-density regions, the system is acting like a periodic state, since the section is temporarily pointlike. We have verified that the laminar regions of a time series (such as in Fig. 6) occur when the system is in one of these regions of high density on the section. A more schematic view of the dynamics on the section is provided in Fig. 12b.

It is possible to gain some insight into the origins of the intermittency from analyzing a 2D map which displays similar behavior:

$$\begin{aligned} \Theta_{n+1} &= \left[\Theta_n + \Omega - \frac{r_n}{2\pi} \sin(2\pi\Theta_n) + Kr_n^2 \right] \bmod 1 \\ r_{n+1} &= r_n \left[1 + \alpha - \alpha \left(\frac{r_n}{R} \right)^2 \right] + \frac{\gamma}{2\pi} \cos(2\pi\Theta_n) \end{aligned} \tag{8}$$

This map is noninvertible and is consequently not a proper model of a flow in a 3D phase space. We do not know, however, of any fundamental reason why similar behavior could not occur in an invertible 2D map, although in practice secondary tori do seem easier to observe numerically in noninvertible maps. To make sure we are not looking at effects due to a phase space dimension greater than three, we have performed fractal dimension analysis of chaotic states just outside the resonance horn. On the lower edge the

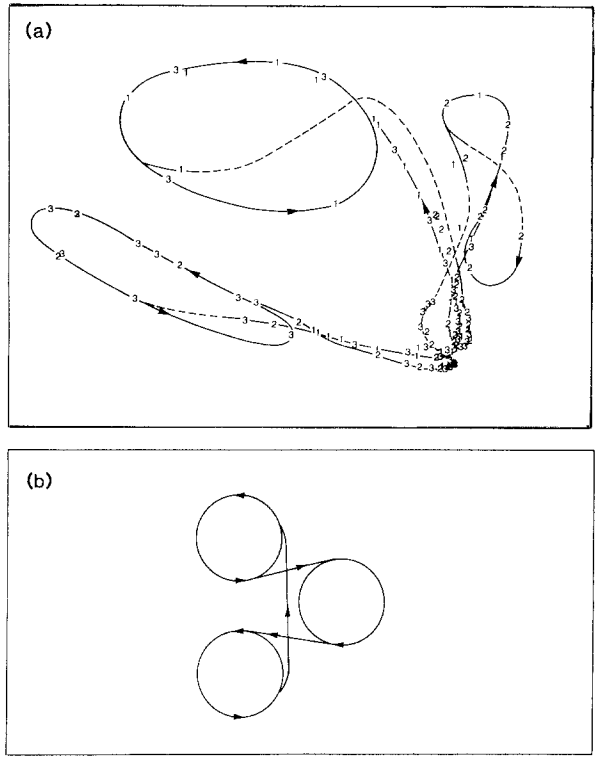

Fig. 12. (a) A Poincaré section just above the onset of intermittency. The points are cyclically labeled 1, 2, 3, 1, 2, 3,... in order of occurrence. Note particularly the regions of high point density in the lower right corner. The lines are guides to the eye, intended to show the iteration sequence of the third-iterate points (1's, 2's, and 3's). The solid lines also should roughly indicate the appearance of the section if infinitely many point were plotted; a dashed line was used in regions of sparse data. (b) A schematic view representing the three iterations and the motion between them. In some data we see a circle traversed several times before the system moves on.

attractor has dimension 2.5 ± 0.1 using the correlation dimension algorithm of Grassberger and Proccacia.[16] This suggests that nearby attractors can be described as flows in 3D phase space and thus by invertible 2D maps.

Using computer code developed by Kevrekidis and co-workers,[12,17] we show two attractors with their fixed points in Fig. 13. Our main desire is to understand the origin of the intermittency, and we will pass over other theoretically interesting properties of these attractors. Figure 13a shows an attractor composed of just three circles. The squares mark the positions of spiral repellers, and the triangles mark the positions of fixed points which have both an attracting direction and a repelling direction (i.e., saddles).

Figure 13b corresponds to a slightly larger nonlinearity, for which the circles have merged into a chaotic attractor. An expanded view would show that the circles are not smooth but instead are composed of many tight folds.

This pair of pictures is intended to help make an analogy between the unlocking transition from periodic to quasiperiodic behavior and the more complex transition from quasiperiodic to chaotic behavior that may describe the experimentally observed intermittency. In simple models of mode locking, the unlocking transition is very similar to intermittency, in that there is a tangent bifurcation similar to that shown in Fig. 11b. In both cases there is a "laminar," nearly-periodic portion of the time series, alter-

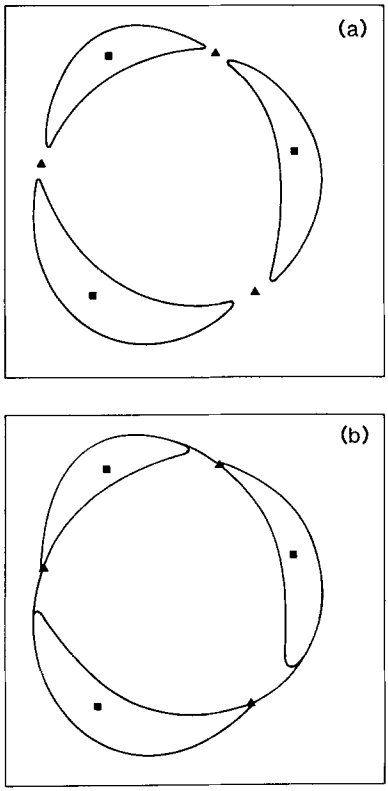

Fig. 13. Two attractors for the map of Eq. (8). The rectangles are repelling fixed points with complex eigenvalues, and the triangles are saddle nodes. (a) A quasiperiodic state with threefold symmetry. Parameter values are $\Omega = 0.25$, $K = 0.15$, $R = 4.0$, $\gamma = 0.42$, and $\alpha = 0.070$. (b) The parameter values are the same as in (a) except $\alpha = 0.073$. This is a chaotic attractor. On a fine scale the circles are no longer smooth, but consist of many large undulations very tightly compressed in a direction perpendicular to the attractor.

nating with more complicated behavior; chaotic behavior in the case of intermittency, and quasiperiodic behavior in the mode-locking case. The presence of chaotic behavior and fractal attractors makes the former case by far the more complicated. But in both instances, the saddles (triangles) collide with the stable attractor to mix together. When the points on the section pass close to a saddle, slow transients and nearly-periodic behavior occur. This analogy, and the data in Fig. 12, suggest a qualitative resemblance to a one-dimensional map [Eq. (3) or (7)], but the reinjection process may be different, and a one-dimensional map perhaps oversimplifies the two-dimensional character of the section. The numeric results indicate that the saddles, and thus the regions of high point density, should lie on the edge of the circles, while this is not apparent in the data.

5. CONCLUSIONS

There are two elements in this transition to intermittent behavior which are important to consider. First, there is the nature of the intermittency itself and how it compares to standard models of such phenomena. There are many qualitative similarities between the experimental data and the type II and type III intermittency models of Pomeau and Manneville.[1] The transition presented here, however, occurs on a mode-locked torus as opposed to on a periodic limit cycle and therefore a simple 1D map analysis may not be relevant. The actual experimental dynamics is complex and probably involves global bifurcations and interactions of stable and unstable manifolds. We presented experimental Poincaré sections and numerical simulations of a 2D map which gave a flavor for this complicated dynamics and its probable source.

The second interesting feature of the data is the ability of externally applied noise to induce the transition to the chaotic state. Again some characteristics of the experiment are qualitatively explained by the numerical models of noise-induced intermittency discussed in this paper. Assuming that our picture of the dynamics of the intermittent state in the absence of external noise is fundamentally correct, then an understanding of the noise-induced transition is also possible. Close to the transition the period-3 secondary tori are only weakly stable and the stable and unstable manifolds which form the separatrices between the period-3 tori are close to overlapping, causing global bifurcation structures.[18] When noise is applied it causes the system to be perturbed out of one of the weakly attracting tori and to hop to another of the period-3 tori. Of course each of the period-3 tori is connected by the flow and what one is actually doing is introducing a random phase disturbance of the period-3 iteration. As the tori become more or less attracting, it becomes more or less difficult for the

system to escape from the basin of attraction of the stable period-3 corresponding, in the experiment, to an increase in the critical noise threshold as $|\delta|$ increases (recall that δ is the distance from the unperturbed transition point).

In conclusion, we have constructed a description of a state of intermittent chaos in a convecting fluid. We have also discussed how this intermittent state can be excited by the application of external noise. Our description includes both global features of the attractor and possible universal aspects of intermittency derived from 1D map models. Further experimental work on the global features of the 2/11 resonance horn would help considerably in understanding this transition.

ACKNOWLEDGMENTS

We would like to acknowledge valuable assistance from I. Kevrekidis in the analysis of our 2D map model. We also thank Tim Sullivan for useful discussions and for a thorough proofreading of this manuscript. This work was supported with funds provided by the Department of Energy, Office of Basic Energy Science, Division of Materials Science.

REFERENCES

1. Y. Pomeau and P. Manneville, *Commun. Math. Phys.* **74**:189 (1980).
2. J. E. Hirsch, B. A. Huberman, and D. J. Scalapino, *Phys. Rev. A* **25**:519 (1982).
3. C. Jefferies and J. Perez, *Phys. Rev. A* **26**:2117 (1982).
4. P. Bergé, M. Dubois, P. Manneville, and Y. Pomeau, *J. Phys. Lett.* (Paris) **41**:L-341 (1980); M. Dubois, M. A. Rubio, and P. Bergé, *Phys. Rev. Lett.* **51**:1446 (1983).
5. J.-P. Eckmann, L. Thomas, and P. Wittwer, *J. Phys. A* **14**:3153 (1981).
6. H. Haucke, R. E. Ecke, Y. Maeno, and J. C. Wheatley, *Phys. Rev. Lett.* **53**:2090 (1984).
7. H. Haucke and R. E. Ecke, *Physica* **25D**:307 (1987).
8. R. E. Ecke and I. G. Kevrekidis, *Phys. Lett. A* **131**:344 (1988).
9. V. Steinberg, *Phys. Rev. A* **24**:975 (1981); A. J. Fetter, *Phys. Rev. B* **26**:1164, 1174 (1982).
10. Y. Maeno, H. Haucke, R. E. Ecke, and J. C. Wheatley, *J. Low Temp. Phys.* **59**:305 (1985).
11. R. E. Ecke, Y. Maeno, H. Haucke, and J. C. Wheatley, *Phys. Rev. Lett.* **53**:1567 (1984); R. E. Ecke, H. Haucke, Y. Maeno, and J. C. Wheatley, *Phys. Rev. A* **33**:1870 (1986); R. J. Deissler, R. E. Ecke, and H. Haucke, *Phys. Rev. A* **36**:4390 (1987).
12. I. G. Kevrekidis and R. E. Ecke, in *SIAM Proceedings of AMS Conference* (Boulder, Colorado, 1987).
13. J.-P. Eckmann and D. Ruelle, *Rev. Mod. Phys.* **57**:617 (1985), and references therein.
14. P. Richetti, F. Argoul, and A. Arneodo, *Phys. Rev. A* **34**:726 (1986).
15. J. Crutchfield, J. D. Farmer, and B. Huberman, *Phys. Rep.* **92**:47 (1982).
16. P. Grassberger and I. Procaccia, *Phys. Rev. Lett.* **50**:346 (1983).
17. I. G. Kevrekidis, R. Aris, L. D. Schmidt, and S. Pelikan, *Physica* **16D**:243 (1985).
18. D. Aronson, M. Chory, G. Hall, and R. McGehee, *Commun. Math. Phys.* **83**:303 (1982).